Nuclear Engineering and Technology 55 (2023) 1350–1364

Contents lists available at ScienceDirect

Nuclear Engineering and Technology

journal homepage: www.elsevier.com/locate/net

Original Article

Convergence study of traditional 2D/1D coupling method for k-eigenvalue neutron transport problems with Fourier analysis

Boran Kong [a], Kaijie Zhu [a], Han Zhang [a,*], Chen Hao [b], Jiong Guo [a], Fu Li [a]

[a] Institute of Nuclear and New Energy Technology (INET), Collaborative Innovation Center of Advanced Nuclear Energy Technology, Key Laboratory of Advanced Reactor Engineering and Safety of Ministry of Education Tsinghua University, Beijing 100084, China
[b] Fundamental Science on Nuclear Safety and Simulation Technology Laboratory, Harbin Engineering University, Harbin, 150001, China

ARTICLE INFO

Article history:
Received 9 July 2022
Received in revised form
20 December 2022
Accepted 25 December 2022
Available online 29 December 2022

Keywords:
Convergence study
2D/1D coupling method
Fourier analysis
Divergence problem
Two SN sweepings

ABSTRACT

2D/1D coupling method is an important neutron transport calculation method due to its high accuracy and relatively low computation cost. However, 2D/1D coupling method may diverge especially in small axial mesh size. To analyze the convergence behavior of 2D/1D coupling method, a Fourier analysis for k-eigenvalue neutron transport problems is implemented. The analysis results present the divergence problem of 2D/1D coupling method in small axial mesh size. Several common attempts are made to solve the divergence problem, which are to increase the number of inner iterations of the 2D or 1D calculation, and two times 1D calculations per outer iteration. However, these attempts only could improve the convergence rate but cannot deal with the divergence problem of 2D/1D coupling method thoroughly. Moreover, the choice of axial solvers, such as DGFEM SN and traditional SN, and its effect on the convergence behavior are also discussed. The results show that the choice of axial solver is a key point for the convergence of 2D/1D method. The DGFEM SN based 2D/1D method could converge within a wide range of optical thickness region, which is superior to that of traditional SN method.
© 2022 Korean Nuclear Society, Published by Elsevier Korea LLC. This is an open access article under the CC BY-NC-ND license (http://creativecommons.org/licenses/by-nc-nd/4.0/).

1. Introduction

2D/1D method couples a radial 2D transport equation and an axial 1D equation for solving the 3D neutron Boltzmann equation. It achieves high accuracy under a relatively low calculation burden. This method was originally developed by two groups in Korea during 2002–2007 [1–3]. One group at KAIST developed 2D/1D fusion method for CRX code [4]. The other one at KAERI developed 2D/1D method for DeCART code [5] and later for nTRACER [6]. In this paper, the 2D/1D coupling method is refer to the 2D/1D method developed at KAERI. Several codes are developed based on 2D/1D coupling method like MPACT [7], NECP-X [8] and HNET [9]. In the early version of DeCART, it meets the divergence problem in small axial mesh size [10]. Similarly, for the 3X3 partially rodded lattice problem, MPACT also suffers from the divergence problem when refining the axial mesh size [11]. To pursue high accuracy, fine axial mesh size is usually required in the 2D/1D coupling method and it may lead to the divergence problem. Therefore, it is necessary to analyze the convergence behavior of 2D/1D coupling method, especially for the fine axial mesh size.

Fourier analysis is an important tool to analyze the asymptotic convergence rate of the iteration [12–19]. A Fourier analysis of 2D/1D coupling method has been implemented for solving 3D k-eigenvalue diffusion problem [29]. With the help of the Fourier analysis, the divergence problem may occur in small axial mesh size. The stability of 2D transport/1D diffusion coupling method is performed by Fourier analysis for the code DeCART [10]. It also shown that the 2D/1D coupling method may fall down the divergence problem. Please note that, in the above work, the diffusion method is used as the 1D solver. While, in this study, the radial and axial transport physics are preserved. This paper focus on the divergence problem of 2D/1D coupling method in small axial mesh size. In practice, two times 1D calculation per 2D/1D outer iteration, as well as the increase of the inner iterations number of 2D or 1D solver, is usually used to improve the convergence rate. In this work, these common attempts are utilized and assessed for solving the divergence problem. Moreover, the choice of axial solvers and its effect on the convergence behavior are also discussed here. The comparison between traditional SN axial solver and Discontinuous Galerkin Finite Element Method based (DGFEM) SN [20] axial solver is performed.

* Corresponding author.
E-mail address: han-zhang@tsinghua.edu.cn (H. Zhang).

https://doi.org/10.1016/j.net.2022.12.034
1738-5733/© 2022 Korean Nuclear Society, Published by Elsevier Korea LLC. This is an open access article under the CC BY-NC-ND license (http://creativecommons.org/licenses/by-nc-nd/4.0/).

The paper is organized as follows. In section 2, the basic theory of 2D/1D iteration scheme is described. Following the iteration scheme, the linearization of the major equations is derived and presented. In section 4, the Fourier analysis of traditional SN based 2D/1D coupling method is derived. The divergence problem of 2D/1D coupling method, as well as the possible tricks, are discussed in section 5. Moreover, the effect of the axial solver on the stability is also analyzed. In section 6, the numerical tests are performed to evaluate the performance of Fourier analysis. Finally, the conclusions are summarized in section 7.

2. Theory of 2D/1D iteration scheme

2.1. Formula of 2D/1D coupling method

The formula of 2D/1D coupling method of the lth iteration are shown as follows. The 2D radial equation is shown in Eq. (1) and 1D axial equation is shown in Eq. (2). These two equations couple with each other by transverse leakage term. Due to the high accuracy and good geometric adaptability, MOC is often applied to solve the 2D transport equation in the practical applications. In Fourier analysis, the traditional 2D SN is often adopted as the radial solver, instead of the MOC, to pursue the simplicity [10,21].

$$2D:\left(\xi_m\frac{\partial}{\partial x}+\eta_m\frac{\partial}{\partial y}\right)\phi_m^Z+\Sigma_t\phi_m^Z=\frac{\Sigma_s}{4\pi}\phi^Z+\frac{\nu\Sigma_f}{4\pi k_{eff}}\phi^Z-TL_{Axial} \tag{1a}$$

$$TL_{Axial}=\frac{\mu_m}{\Delta_z}\left(\phi_m^T-\phi_m^B\right)=\frac{1}{4\pi\Delta_z}\left(J^{top}-J^{bottom}\right) \tag{1b}$$

$$1D:\mu_m\frac{\partial}{\partial z}\phi_m^{XY}+\Sigma_t\phi_m^{XY}=\frac{\Sigma_s}{4\pi}\phi^{XY}+\frac{\nu\Sigma_f}{4\pi k_{eff}}\phi^{XY}-TL_{Radial} \tag{2a}$$

$$TL_{Radial}=\frac{\xi_m}{\Delta}\left(\phi_m^{x_R}-\phi_m^{x_L}\right)+\frac{\eta_m}{\Delta}\left(\phi_m^{y_R}-\phi_m^{y_L}\right)=\frac{1}{4\pi\Delta}\left(J^{x_R}-J^{x_L}+J^{y_R}-J^{y_L}\right) \tag{2b}$$

Where μ, η, ξ are the angle of Z, Y and X direction respectively. ϕ is the angular flux, andϕ is the scalar flux.Σ_t, Σ_s, Σ_f is total cross-section, scattering cross-section, fission cross-section respectively. ν is the number of fission neutrons per fission, k_{eff} is the effective eigenvalue, J is the net current,Δ is the coarse mesh radial size, and Δ_z is the coarse mesh axial size. The superscript Z represents that the variable is axially averaged and XY represents that the variable is radially averaged. The superscript top, bottom represent the coarse-mesh top and bottom boundary, x_L, x_R, y_L, y_R are the coarse-mesh left and right boundary in X and Y direction respectively. The subscript m represents the discrete angular. TL_{Axial} is the axial transverse leakage and TL_{Radial} is the radial transverse leakage. Here, the isotropic transverse leakage term is applied, which is calculated by the net current. Isotropic scattering source term and fission source term are also used for simplicity.

The flow chart of the 2D/1D iteration scheme for the k-eigenvalue neutron transport problem is shown in Fig. 1. Specifically, there are twice 1D axial SN, a radial SN and a 3D adCMFD acceleration [8,13,22] in each outer iteration. For the l^{th} outer iteration, according to the 2D/1D iteration scheme, the radial transverse leakage for the first time 1D axial SN is calculated from the $(l-1)^{\text{th}}$ CMFD. While, the axial transverse leakage is calculated from the l^{th} first-time 1D axial SN calculation. The radial transverse leakage for the second 1D axial SN is calculated froml^{th} 2D radial SN calculation. For the first 1D axial SN calculation, the number of inner iteration (sweep) refers to N_1. Similarly, the number of inner iteration (sweep) of 2D radial SN and the second 1D axial SN calculation are N_2 and N_1, respectively. Also, the indexes of the inner iteration are set as n_1, n_2 and n_3 respectively. During the inner iteration, the scattering source updates, while, the transverse leakage term and fission source term keep as constant.

The spatial discretization of the 2D/1D coupling method is shown in Fig. 2. Axially, the number of fine meshes per coarse mesh is p. Radially, the number of fine meshes per coarse mesh is p^2. In Fig. 2, the p is set as 3 for example. I, J, K represent the index of coarse mesh in X, Y, Z direction respectively.

Using SN method, the 2D equation is discretized as follows for the 2D cartesian square mesh:

$$\frac{\xi_m}{h_1}\left(\phi_{m,i+\frac{1}{2},j,K}^{l+\frac{1}{2},n_2+1}-\phi_{m,i-\frac{1}{2},j,K}^{l+\frac{1}{2},n_2+1}\right)+\frac{\eta_m}{h_1}\left(\phi_{m,i,j+\frac{1}{2},K}^{l+\frac{1}{2},n_2+1}-\phi_{m,i,j-\frac{1}{2},K}^{l+\frac{1}{2},n_2+1}\right)+\Sigma_t\phi_{m,i,j,K}^{l+\frac{1}{2},n_2+1}=\frac{\Sigma_s}{4\pi}\phi_{i,j,K}^{l,n_2}+\frac{\nu\Sigma_f}{4\pi k_{eff}^l}\phi_{i,j,K}^l-\frac{1}{4\pi\Delta_z}\left(J_{I,J,K}^{top}-J_{I,J,K}^{bottom}\right) \tag{3a}$$

$$h_1=\Delta/p \tag{3b}$$

Where the subscripts i, j represent the index of fine mesh in the coarse mesh in X, Y direction, respectively. The subscript K represents that the equation is axially averaged on coarse mesh K. $i+\frac{1}{2}$ and $i-\frac{1}{2}$ are the fine mesh right and left boundary in X direction, and $j+\frac{1}{2}$ and $j-\frac{1}{2}$ are the boundary in Y direction. n_2 represents the n_2^{th} inner iteration of scattering source, and h_1 is the fine mesh radial size. After one inner iteration, a new axially averaged scalar flux is obtained by the updated angular flux:

$$\phi_{i,j,K}^{l+\frac{1}{2},n_2+1}=\sum_{m=1}^{M}w_m\phi_{m,i,j,K}^{l+\frac{1}{2},n_2+1} \tag{4}$$

It should be noted that the scalar flux calculated from 2D equation is the axially averaged value of the fine mesh (i, j, K). SN discretization needs supplement equation which is:

$$\left(\phi_{m,i+\frac{1}{2},j,K}^{l+\frac{1}{2},n_2+1}+\phi_{m,i-\frac{1}{2},j,K}^{l+\frac{1}{2},n_2+1}\right)-\left(\phi_{m,i,j+\frac{1}{2},K}^{l+\frac{1}{2},n_2+1}+\phi_{m,i,j-\frac{1}{2},K}^{l+\frac{1}{2},n_2+1}\right)=0 \tag{5}$$

Here, diamond difference (DD) format is applied. The central angular flux of the fine mesh (i, j, K) can be represented by the boundary angular flux, which is:

$$\phi_{m,i,j,K}^{l+\frac{1}{2},n_2+1}=\frac{1}{4}\left(\phi_{m,i+\frac{1}{2},j,K}^{l+\frac{1}{2},n_2+1}+\phi_{m,i-\frac{1}{2},j,K}^{l+\frac{1}{2},n_2+1}+\phi_{m,i,j+\frac{1}{2},K}^{l+\frac{1}{2},n_2+1}+\phi_{m,i,j-\frac{1}{2},K}^{l+\frac{1}{2},n_2+1}\right) \tag{6}$$

Eq. (6) is substituted into Eq. (3), then the 2D equation becomes:

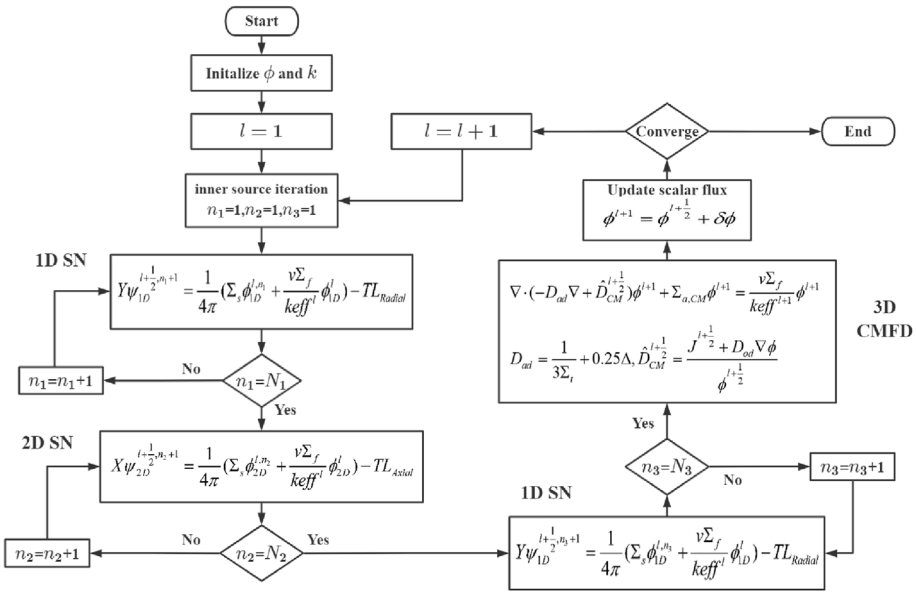

Fig. 1. Flow chart of 2D/1D iteration scheme for k-eigenvalue problems.

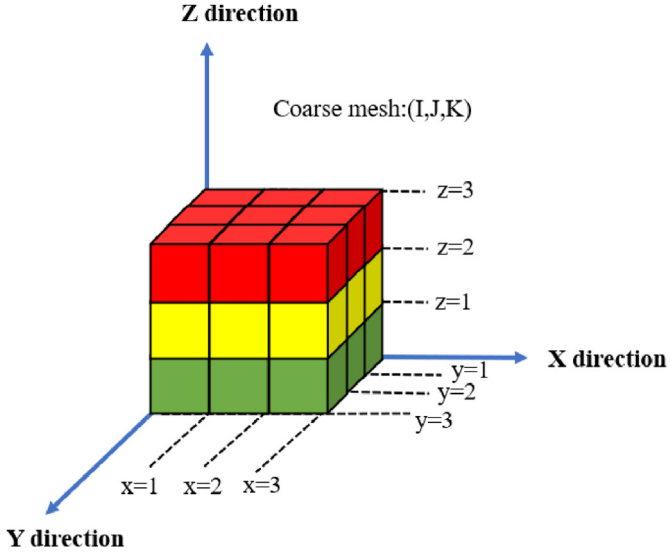

Fig. 2. Square meshes of 2D/1D coupling method.

$$\frac{\xi_m}{h_1}\left(\phi_{m,i+\frac{1}{2},j,K}^{l+\frac{1}{2},n_2+1}-\phi_{m,i-\frac{1}{2},j,K}^{l+\frac{1}{2},n_2+1}\right)+\frac{\eta_m}{h_1}\left(\phi_{m,i,j+\frac{1}{2},K}^{l+\frac{1}{2},n_2+1}-\phi_{m,i,j-\frac{1}{2},K}^{l+\frac{1}{2},n_2+1}\right)$$
$$+\frac{\Sigma_t}{4}\left(\phi_{m,i+\frac{1}{2},j,K}^{l+\frac{1}{2},n_2+1}+\phi_{m,i-\frac{1}{2},j,K}^{l+\frac{1}{2},n_2+1}+\phi_{m,i,j+\frac{1}{2},K}^{l+\frac{1}{2},n_2+1}+\phi_{m,i,j-\frac{1}{2},K}^{l+\frac{1}{2},n_2+1}\right) \tag{7a}$$
$$=\frac{\Sigma_s}{4\pi}\phi_{i,j,K}^{l,n_2}+\frac{\nu\Sigma_f}{4\pi k_{eff}^l}\phi_{i,j,K}^l+TL_{axial}$$

$$TL_{axial}=-\frac{1}{4\pi\Delta_z}\left(J_{I,J,K}^{top}-J_{I,J,K}^{bottom}\right) \tag{7b}$$

Similar as 2D equation, using SN, the 1D equation can be discretized as follows for the 1D cartesian square mesh:

$$\frac{\mu_m}{h_2}\left(\phi_{m,I,J,k+\frac{1}{2}}^{l+\frac{1}{2},n+1}-\phi_{m,I,J,k-\frac{1}{2}}^{l+\frac{1}{2},n+1}\right)+\Sigma_t\phi_{m,I,J,k}^{l+\frac{1}{2},n+1}=\frac{\Sigma_s}{4\pi}\phi_{I,J,k}^{l,n}+\frac{\nu\Sigma_f}{4\pi k_{eff}^l}\phi_{I,J,k}^l$$
$$-\frac{1}{4\pi\Delta}\left(J_{I,J,K}^{x_R}-J_{I,J,K}^{x_L}+J_{I,J,K}^{y_R}-J_{I,J,K}^{y_L}\right) \tag{8a}$$

$$h_2=\Delta_z/p \tag{8b}$$

Where the subscripts I and J represent that the equation is radially averaged on coarse mesh (I, J). $k+\frac{1}{2}$ and $k-\frac{1}{2}$ are the fine mesh top and bottom boundary. n denotes the nth inner iteration of scattering source. After one inner iteration, a new radially averaged scalar flux can be updated by the angular flux:

$$\phi_{I,J,k}^{l+\frac{1}{2},n+1}=\sum_{m=1}^{M}w_m\phi_{m,I,J,k}^{l+\frac{1}{2},n+1} \tag{9}$$

The central angular flux of the fine mesh (I, J, k) is presented by the boundary angular flux using DD format, which is:

$$\phi_{m,I,J,k}^{l+\frac{1}{2},n+1}=\frac{1}{2}\left(\phi_{m,I,J,k+\frac{1}{2}}^{l+\frac{1}{2},n+1}+\phi_{m,I,J,k-\frac{1}{2}}^{l+\frac{1}{2},n+1}\right) \tag{10}$$

Substituting Eq. (10) into Eq. (8), then the 1D equation becomes:

$$\frac{\mu_m}{h_2}\left(\phi_{m,I,J,k+\frac{1}{2}}^{l+\frac{1}{2},n+1}-\phi_{m,I,J,k-\frac{1}{2}}^{l+\frac{1}{2},n+1}\right)+\frac{\Sigma_t}{2}\left(\phi_{m,I,J,k+\frac{1}{2}}^{l+\frac{1}{2},n+1}+\phi_{m,I,J,k-\frac{1}{2}}^{l+\frac{1}{2},n+1}\right)$$
$$=\frac{\Sigma_s}{4\pi}\phi_{I,J,k}^{l,n}+\frac{\nu\Sigma_f}{4\pi k_{eff}^l}\phi_{I,J,k}^l+TL_{radial} \tag{11a}$$

$$TL_{radial}=-\frac{1}{4\pi\Delta}\left(J_{I,J,K}^{x_R}-J_{I,J,K}^{x_L}+J_{I,J,K}^{y_R}-J_{I,J,K}^{y_L}\right) \tag{11b}$$

Then the coarse-mesh scalar flux is updated by solving the

artificially diffusive CMFD (adCMFD) equation:

$$\frac{1}{\Delta}\left(J^{l+1}_{I+\frac{1}{2}J,K}-J^{l+1}_{I-\frac{1}{2}J,K}\right)+\frac{1}{\Delta}\left(J^{l+1}_{IJ+\frac{1}{2},K}-J^{l+1}_{IJ-\frac{1}{2},K}\right)+\frac{1}{\Delta_z}\left(J^{l+1}_{IJ,K+\frac{1}{2}}-J^{l+1}_{IJ,K-\frac{1}{2}}\right)+\Sigma_{a,CM}\phi^{l+1}_{IJ,K}=\frac{\nu\Sigma_{f,CM}}{keff^{l+1}}\phi^{l+1}_{IJ,K} \tag{12}$$

Where $I\pm\frac{1}{2}$, $J\pm\frac{1}{2}$ and $K\pm\frac{1}{2}$ represent the left and right edge of coarse mesh in X, Y, Z direction respectively. The boundary current J is calculated by Eq. (13a) and Eq. (13b), here the Z direction is taken as example. While, the X and Y direction is similar.

$$J^{l+1}_{IJ,K+\frac{1}{2}}=-\frac{D_{ad}}{\Delta_z}\left(\phi^{l+1}_{IJ,K+1}-\phi^{l+1}_{IJ,K}\right)+\widehat{D}^{l+\frac{1}{2}}_{IJ,K+\frac{1}{2}}\left(\phi^{l+1}_{IJ,K+1}+\phi^{l+1}_{IJ,K}\right) \tag{13a}$$

$$J^{l+1}_{IJ,K-\frac{1}{2}}=-\frac{D_{ad}}{\Delta_z}\left(\phi^{l+1}_{IJ,K}-\phi^{l+1}_{IJ,K-1}\right)+\widehat{D}^{l+\frac{1}{2}}_{IJ,K-\frac{1}{2}}\left(\phi^{l+1}_{IJ,K}+\phi^{l+1}_{IJ,K-1}\right) \tag{13b}$$

Different from the traditional CMFD, adCMFD applies an artificially diffusive coefficient, which is:

$$D_{ad}=\frac{1}{3\Sigma_{t,\mathrm{CM}}}+\theta\Delta \tag{14}$$

θ is called the artificially diffusive coefficient, and here it is set as 0.25. The $\widehat{D}^{l+\frac{1}{2}}_{IJ,K\pm\frac{1}{2}}$ is calculated from the boundary net current calculated from 2D radial SN and 1D axial SN, which is:

$$\widehat{D}^{l+\frac{1}{2}}_{IJ,K+\frac{1}{2}}=\frac{J^{l+\frac{1}{2}}_{IJ,K+\frac{1}{2}}+\frac{D_{ad}}{\Delta_z}\left(\phi^{l+\frac{1}{2}}_{IJ,K+1}-\phi^{l+\frac{1}{2}}_{IJ,K}\right)}{\phi^{l+\frac{1}{2}}_{IJ,K+1}+\phi^{l+\frac{1}{2}}_{IJ,K}} \tag{15a}$$

$$\widehat{D}^{l+\frac{1}{2}}_{IJ,K-\frac{1}{2}}=\frac{J^{l+\frac{1}{2}}_{IJ,K-\frac{1}{2}}+\frac{D_{ad}}{\Delta_z}\left(\phi^{l+\frac{1}{2}}_{IJ,K}-\phi^{l+\frac{1}{2}}_{IJ,K-1}\right)}{\phi^{l+\frac{1}{2}}_{IJ,K}+\phi^{l+\frac{1}{2}}_{IJ,K-1}} \tag{15b}$$

After the adCMFD calculation, the fine mesh scalar flux of 2D radial SN and 1D axial SN are updated by the coarse mesh scalar flux of CMFD, which is:

$$\phi^{l+1}_{i,j,k}=\phi^{l+\frac{1}{2}}_{i,j,k}\frac{\phi^{l+1}_{IJ,K}}{\phi^{l+\frac{1}{2}}_{IJ,K}},(i,j,k)\in(I,J,K) \tag{16}$$

3. Linearization

In order to perform Fourier analysis to evaluate the performance of 2D/1D coupling method, the 2D SN Eq. (7), 1D SN Eq. (11), 3D adCMFD Eq. (12), as well as the scalar updated process Eq. (16) are linearized near the exact solution. The solutions are expressed as a function of error term $\varepsilon\ll1$ for a 3D homogeneous medium k-eigenvalue problem.

$$\phi^{l+\frac{1}{2},n_2}_{m,i,j,K}=\frac{1}{4\pi}+\varepsilon\tilde{\phi}^{l+\frac{1}{2},n_2}_{m,i,j,K} \tag{17a}$$

$$\phi^{l+\frac{1}{2},n_2}_{m,i\pm\frac{1}{2}j\pm\frac{1}{2},K}=\frac{1}{4\pi}+\varepsilon\tilde{\phi}^{l+\frac{1}{2},n_2}_{m,i\pm\frac{1}{2}j\pm\frac{1}{2},K} \tag{17b}$$

$$\phi^{l+\frac{1}{2},n}_{m,I,J,k}=\frac{1}{4\pi}+\varepsilon\tilde{\phi}^{l+\frac{1}{2},n}_{m,I,J,k} \tag{17c}$$

$$\phi^{l+\frac{1}{2},n}_{m,I,J,k\pm\frac{1}{2}}=\frac{1}{4\pi}+\varepsilon\tilde{\phi}^{l+\frac{1}{2},n}_{m,I,J,k\pm\frac{1}{2}} \tag{17d}$$

$$\phi^{l+\frac{1}{2}}_{I,J,k}=1+\varepsilon\tilde{\phi}^{l+\frac{1}{2}}_{I,J,k} \tag{17e}$$

$$\phi^{l+\frac{1}{2}}_{i,j,K}=1+\varepsilon\tilde{\phi}^{l+\frac{1}{2}}_{i,j,K} \tag{17f}$$

$$\phi^{l+\frac{1}{2}}_{IJ,K}=1+\varepsilon\tilde{\phi}^{l+\frac{1}{2}}_{IJ,K} \tag{17g}$$

$$J^{l+\frac{1}{2}}_{I\pm\frac{1}{2}J\pm\frac{1}{2},K\pm\frac{1}{2}}=0+\varepsilon\tilde{J}^{l+\frac{1}{2}}_{I\pm\frac{1}{2}J\pm\frac{1}{2},K\pm\frac{1}{2}} \tag{17h}$$

$$J^{l+1}_{I\pm\frac{1}{2}J\pm\frac{1}{2},K\pm\frac{1}{2}}=0+\varepsilon\tilde{J}^{l+1}_{I\pm\frac{1}{2}J\pm\frac{1}{2},K\pm\frac{1}{2}} \tag{17i}$$

$$\widehat{D}^{l+\frac{1}{2}}_{I+\frac{1}{2}J\pm\frac{1}{2},K\pm\frac{1}{2}}=0+\varepsilon\tilde{D}^{l+\frac{1}{2}}_{I+\frac{1}{2}J\pm\frac{1}{2},K\pm\frac{1}{2}} \tag{17j}$$

$$\frac{1}{keff^{l+1}}=\frac{\Sigma_a}{\nu\Sigma_f}+\varepsilon\zeta^{l+1} \tag{17k}$$

By summing up all the coarse meshes, it can be obtained that:

$$\varepsilon\zeta^{l+1}=0 \tag{18}$$

For the first 1D axial SN calculation as shown in Fig. 1, the radial transverse leakage term is calculated from the CMFD calculation and the formula is shown in Eq. (19a). Substituting Eq. (17c, d, e) into 1D axial Eq. (11), the linearized equation becomes Eq. (19b):

$$TL_{radial}=\frac{1}{4\pi\Delta}\left(J_{I+\frac{1}{2}J,K}-J_{I-\frac{1}{2}J,K}+J_{IJ+\frac{1}{2},K}-J_{IJ-\frac{1}{2},K}\right) \tag{19a}$$

$$\frac{\mu_m}{h_2}\left(\tilde{\phi}^{l+\frac{1}{2},n_1+1}_{m,IJ,k+\frac{1}{2}}-\tilde{\phi}^{l+\frac{1}{2},n_1+1}_{m,IJ,k-\frac{1}{2}}\right)+\frac{\Sigma_t}{2}\left(\tilde{\phi}^{l+\frac{1}{2},n_1+1}_{m,IJ,k+\frac{1}{2}}+\tilde{\phi}^{l+\frac{1}{2},n_1+1}_{m,IJ,k-\frac{1}{2}}\right)=\frac{\Sigma_s}{4\pi}\tilde{\phi}^{l,n_1}_{IJ,k}+\frac{\Sigma_a}{4\pi}\tilde{\phi}^{l}_{IJ,k}-\frac{1}{4\pi\Delta}\left(\tilde{J}_{I+\frac{1}{2}J,K}-\tilde{J}_{I-\frac{1}{2}J,K}+\tilde{J}_{IJ+\frac{1}{2},K}-\tilde{J}_{IJ-\frac{1}{2},K}\right) \tag{19b}$$

For the second 1D axial SN calculation, the radial transverse leakage term is calculated from the 2D radial calculation, taking the

left boundary net current in X-direction for example:

$$J^{x_L}_{I,J,K}=\frac{1}{p}\sum_{m=1}^{M}\sum_{j=1}^{P}w_m\xi_m\phi^{l,N_2}_{m,0,J,K} \tag{20}$$

For brief, the error term of the net current is simplified as:

$$\tilde{J}^{x_L}_{I,J,K}=\frac{1}{p}\sum_{m=1}^{M}\sum_{j=1}^{P}w_m\xi_m\tilde{\phi}^{l,N_2}_{m,0,J,K} \tag{21}$$

The linearized second 1D axial SN calculation is as follows:

$$\begin{aligned}&\frac{\mu_m}{h_2}\left(\tilde{\phi}^{l+\frac{1}{2},n_3+1}_{m,I,J,k+\frac{1}{2}}-\tilde{\phi}^{l+\frac{1}{2},n_3+1}_{m,I,J,k-\frac{1}{2}}\right)+\frac{\Sigma_t}{2}\left(\tilde{\phi}^{l+\frac{1}{2},n_3+1}_{m,I,J,k+\frac{1}{2}}+\tilde{\phi}^{l+\frac{1}{2},n_3+1}_{m,I,J,k-\frac{1}{2}}\right)\\&=\frac{\Sigma_s}{4\pi}\tilde{\phi}^{l,n_3}_{I,J,k}+\frac{\Sigma_a}{4\pi}\tilde{\phi}^{l}_{I,J,k}-\frac{1}{4\pi\Delta}\left(\tilde{J}^{x_R}_{I,J,K}-\tilde{J}^{x_L}_{I,J,K}+\tilde{J}^{y_R}_{I,J,K}-\tilde{J}^{y_L}_{I,J,K}\right)\end{aligned} \tag{22}$$

Eq. (17a, b, f) is substituted into 2D radial Eq. (7), then the linearized 2D equation becomes Eq. (23):

$$\begin{aligned}&\frac{\xi_m}{h_1}\left(\tilde{\phi}^{l+\frac{1}{2},n_2+1}_{m,i+\frac{1}{2},j,K}-\tilde{\phi}^{l+\frac{1}{2},n_2+1}_{m,i-\frac{1}{2},j,K}\right)+\frac{\eta_m}{h_1}\left(\tilde{\phi}^{l+\frac{1}{2},n_2+1}_{m,i,j+\frac{1}{2},K}-\tilde{\phi}^{l+\frac{1}{2},n_2+1}_{m,i,j-\frac{1}{2},K}\right)\\&+\frac{\Sigma_t}{4}\left(\tilde{\phi}^{l+\frac{1}{2},n_2+1}_{m,i+\frac{1}{2},j,K}+\tilde{\phi}^{l+\frac{1}{2},n_2+1}_{m,i-\frac{1}{2},j,K}+\tilde{\phi}^{l+\frac{1}{2},n_2+1}_{m,i,j+\frac{1}{2},K}+\tilde{\phi}^{l+\frac{1}{2},n_2+1}_{m,i,j-\frac{1}{2},K}\right)\\&=\frac{\Sigma_s}{4\pi}\tilde{\phi}^{l,n_2}_{i,j,K}+\frac{\Sigma_a}{4\pi}\tilde{\phi}^{l}_{i,j,K}-\frac{1}{4\pi\Delta_z}\left(\tilde{J}^{top}_{I,J,K}-\tilde{J}^{bottom}_{I,J,K}\right)\end{aligned} \tag{23}$$

After two 1D calculations and one 2D radial calculation, the net current of the coarse mesh is obtained using Eq. (13) and Eq. (15). Substituting Eq. (17h-j) into Eq. (13), the linearized net current becomes:

$$\tilde{J}^{l+1}_{I,J,K+\frac{1}{2}}=-\frac{D_{ad}}{\Delta_z}\left(\tilde{\phi}^{l+1}_{I,J,K+1}-\tilde{\phi}^{l+1}_{I,J,K}\right)+\frac{D_{ad}}{\Delta_z}\left(\tilde{\phi}^{l+\frac{1}{2}}_{I,J,K+1}-\tilde{\phi}^{l+\frac{1}{2}}_{I,J,K}\right)+\tilde{J}^{l+\frac{1}{2}}_{I,J,K+\frac{1}{2}} \tag{24a}$$

$$\tilde{J}^{l+1}_{I,J,K-\frac{1}{2}}=-\frac{D_{ad}}{\Delta_z}\left(\tilde{\phi}^{l+1}_{I,J,K}-\tilde{\phi}^{l+1}_{I,J,K-1}\right)+\frac{D_{ad}}{\Delta_z}\left(\tilde{\phi}^{l+\frac{1}{2}}_{I,J,K}-\tilde{\phi}^{l+\frac{1}{2}}_{I,J,K-1}\right)+\tilde{J}^{l+\frac{1}{2}}_{I,J,K-\frac{1}{2}} \tag{24b}$$

Then the net currents are substituted into the 3D CMFD Eq. (12), the linearized form of the CMFD equation is presented as:

$$\begin{aligned}&\frac{\Delta_z}{D_{ad}}\left(\tilde{J}^{l+\frac{1}{2}}_{I+\frac{1}{2},J,K}-\tilde{J}^{l+\frac{1}{2}}_{I-\frac{1}{2},J,K}+\tilde{J}^{l+\frac{1}{2}}_{I,J+\frac{1}{2},K}-\tilde{J}^{l+\frac{1}{2}}_{I,J-\frac{1}{2},K}\right)+\frac{\Delta}{D_{ad}}\left(\tilde{J}^{l+\frac{1}{2}}_{I,J,K+\frac{1}{2}}-\tilde{J}^{l+\frac{1}{2}}_{I,J,K-\frac{1}{2}}\right)+\frac{\Delta_z}{\Delta}\left(\tilde{\phi}^{l+\frac{1}{2}}_{I+1,J,K}-\tilde{\phi}^{l+\frac{1}{2}}_{I-1,J,K}+\tilde{\phi}^{l+\frac{1}{2}}_{I,J+1,K}-\tilde{\phi}^{l+\frac{1}{2}}_{I,J-1,K}-4\tilde{\phi}^{l+1}_{I,J,K}\right)\\&+\frac{\Delta}{\Delta_z}\left(\tilde{\phi}^{l+\frac{1}{2}}_{I,J,K+1}-\tilde{\phi}^{l+\frac{1}{2}}_{I,J,K-1}-2\tilde{\phi}^{l+\frac{1}{2}}_{I,J,K}\right)=\frac{\Delta_z}{\Delta}\left(\tilde{\phi}^{l+1}_{I+1,J,K}-\tilde{\phi}^{l+1}_{I-1,J,K}+\tilde{\phi}^{l+1}_{I,J+1,K}-\tilde{\phi}^{l+1}_{I,J-1,K}-4\tilde{\phi}^{l+1}_{I,J,K}\right)+\frac{\Delta}{\Delta_z}\left(\tilde{\phi}^{l+1}_{I,J,K+1}-\tilde{\phi}^{l+1}_{I,J,K-1}-2\tilde{\phi}^{l+1}_{I,J,K}\right)\end{aligned} \tag{25}$$

The fine-mesh scalar fluxes of 1D axial meshes and 2D radial meshes are updated by the CMFD coarse-mesh scalar flux using Eq. (16). The linearized form of Eq. (16) is:

$$\tilde{\phi}^{l+1}_{i,j,k}=\tilde{\phi}^{l+\frac{1}{2}}_{i,j,k}+\tilde{\phi}^{l+1}_{I,J,K}-\tilde{\phi}^{l+\frac{1}{2}}_{I,J,K},\ (i,j,k)\in(I,J,K) \tag{26}$$

4. Fourier analysis

To theoretically analyze the convergence rate of the iteration, Fourier analysis is usually applied [16,17]. The first step of the Fourier analysis is the linearization near the exact solutions, which is derived in Section 3. The error terms of the linearized equations are expressed as Fourier mode in X, Y, Z direction, and then the error transition matrix can be obtained. The spectral radius of the error transition matrix indicates the convergence rate of the iteration. The Fourier analysis is carried out in one single coarse mesh with periodic boundary conditions [16–19]. Following the standard Fourier analysis, the Fourier ansatz expands the error terms as a function of Fourier frequency as Eq. (27):

$$\tilde{\phi}^{l+\frac{1}{2},n_2}_{m,i,j,K}=A^{l+\frac{1}{2},n_2}_{m,i,j,K}e^{i\Sigma_t\lambda_x x_i}e^{i\Sigma_t\lambda_y y_j}e^{i\Sigma_t\lambda_z z_k} \tag{27a}$$

$$\tilde{\phi}^{l+\frac{1}{2},n_2}_{m,i\pm\frac{1}{2},j\pm\frac{1}{2},K}=A^{l+\frac{1}{2},n_2}_{m,i\pm\frac{1}{2},j\pm\frac{1}{2},K}e^{i\Sigma_t\lambda_x x_i}e^{i\Sigma_t\lambda_y y_j}e^{i\Sigma_t\lambda_z z_k} \tag{27b}$$

$$\tilde{\phi}^{l+\frac{1}{2},n}_{m,I,J,k}=B^{l+\frac{1}{2},n}_{m,I,J,k}e^{i\Sigma_t\lambda_x x_i}e^{i\Sigma_t\lambda_y y_j}e^{i\Sigma_t\lambda_z z_k} \tag{27c}$$

$$\tilde{\phi}^{l+\frac{1}{2},n}_{m,I,J,k\pm\frac{1}{2}}=B^{l+\frac{1}{2},n}_{m,I,J,k\pm\frac{1}{2}}e^{i\Sigma_t\lambda_x x_i}e^{i\Sigma_t\lambda_y y_j}e^{i\Sigma_t\lambda_z z_k} \tag{27d}$$

$$\tilde{\phi}^{l+\frac{1}{2}}_{i,j,K}=C^{l+\frac{1}{2}}_{i,j,K}e^{i\Sigma_t\lambda_x x_i}e^{i\Sigma_t\lambda_y y_j}e^{i\Sigma_t\lambda_z z_k} \tag{27e}$$

$$\tilde{\phi}^{l+\frac{1}{2}}_{I,J,k}=D^{l+\frac{1}{2}}_{I,J,k}e^{i\Sigma_t\lambda_x x_i}e^{i\Sigma_t\lambda_y y_j}e^{i\Sigma_t\lambda_z z_k} \tag{27f}$$

$$\tilde{\phi}^{l+\frac{1}{2}}_{I,J,K}=E^{l+\frac{1}{2}}e^{i\Sigma_t\lambda_x x_i}e^{i\Sigma_t\lambda_y y_j}e^{i\Sigma_t\lambda_z z_k} \tag{27g}$$

$$\tilde{\phi}^{l+1}_{I,J,K}=F^{l+1}e^{i\Sigma_t\lambda_x x_i}e^{i\Sigma_t\lambda_y y_j}e^{i\Sigma_t\lambda_z z_k} \tag{27h}$$

$$\tilde{J}^{l+\frac{1}{2}}_{I\pm\frac{1}{2},J\pm\frac{1}{2},K\pm\frac{1}{2}}=G^{l+\frac{1}{2}}_{I\pm\frac{1}{2},J\pm\frac{1}{2},K\pm\frac{1}{2}}e^{i\Sigma_t\lambda_x x_i}e^{i\Sigma_t\lambda_y y_j}e^{i\Sigma_t\lambda_z z_k} \tag{27i}$$

$$\tilde{J}^{l+1}_{I\pm\frac{1}{2},J\pm\frac{1}{2},K\pm\frac{1}{2}}=H^{l+1}_{I\pm\frac{1}{2},J\pm\frac{1}{2},K\pm\frac{1}{2}}e^{i\Sigma_t\lambda_x x_i}e^{i\Sigma_t\lambda_y y_j}e^{i\Sigma_t\lambda_z z_k} \tag{27j}$$

The essential part of the Fourier analysis is to derive the

transition matrix of the fine-mesh scalar flux error term. In the 2D/1D coupling method, the fine-mesh scalar flux errors contain two parts, which are p^2 number 2D radial fine mesh scalar flux errors and p number 1D axial fine mesh scalar flux errors. These two scalar flux errors are expressed by Fourier ansatz in Eq. (27e) and Eq. (27f). The vector S^l is defined, which stores the 2D radial fine-mesh scalar flux errors and 1D axial fine-mesh scalar flux errors as shown in Eq. (28). The first p elements are the 1D axial fine-mesh scalar flux errors and the next p^2 elements are the 2D radial fine-mesh scalar flux errors.

$$S^l = \begin{bmatrix} \tilde{\phi}^l_{I,J,1} \\ \cdots \\ \tilde{\phi}^l_{I,J,p} \\ \tilde{\phi}^l_{1,1,K} \\ \cdots \\ \tilde{\phi}^l_{p,p,K} \end{bmatrix}_{(p+p^2)\times 1} \tag{28}$$

The vector $B_m^{l+\frac{1}{2},n}$ contains p number boundary angular flux errors of the 1D axial fine-mesh as shown in Eq. (29).

$$B^{l+\frac{1}{2},n}_{m,I,J,k\pm\frac{1}{2}} = \begin{bmatrix} \tilde{\phi}^{l+\frac{1}{2},n}_{m,I,J,\frac{1}{2}} \\ \cdots \\ \tilde{\phi}^{l+\frac{1}{2},n}_{m,I,J,\frac{2p-1}{2}} \end{bmatrix}_{p\times 1} \tag{29}$$

Fourier ansatz is applied into the first-time linearized 1D Eq. (19b). At lth source iteration calculation step, the $l+\frac{1}{2}$ intermediate step boundary angular flux $B^{l+\frac{1}{2},n_1+1}_{m,I,J,k\pm\frac{1}{2}}$ of 1D axial SN is obtained as follows:

$$B^{l+\frac{1}{2},n_1+1}_{m,I,J,k\pm\frac{1}{2}} = Y_m^{-1}\left(C_1E_1S^{l,n_1} + C_2E_1S^l + C_3S^l\right) \tag{30}$$

Where Y_m is a matrix of the 1D axial SN transport calculation with the size of $p \times p$, C_1 is the matrix of the scattering source error term, C_2 is the matrix of the absorption error term, and C_3 is the matrix of the radial transverse leakage error term. E_1 is the transform matrix that convert the scalar flux error matrix of 2D/1D into the matrix of 1D SN scalar flux error, and E is the identity matrix. The detailed expressions of the matrices are:

$$Y_m = \begin{bmatrix} \frac{-\mu_m}{h_2}+\frac{\Sigma_t}{2} & \frac{\mu_m}{h_2}+\frac{\Sigma_t}{2} & 0 & 0 & 0 \\ 0 & \frac{-\mu_m}{h_2}+\frac{\Sigma_t}{2} & \frac{\mu_m}{h_2}+\frac{\Sigma_t}{2} & 0 & 0 \\ \cdots & \cdots & \cdots & \cdots & \cdots \\ \left(\frac{\mu_m}{h_2}+\frac{\Sigma_t}{2}\right)e^{i\Sigma_t\lambda_z\Delta} & 0 & 0 & 0 & \frac{-\mu_m}{h_2}+\frac{\Sigma_t}{2} \end{bmatrix}_{p\times p} \tag{31a}$$

$$C_1 = \begin{bmatrix} \frac{\Sigma_s}{4\pi} & 0 & 0 & 0 & 0 \\ 0 & \frac{\Sigma_s}{4\pi} & 0 & 0 & 0 \\ 0 & 0 & \frac{\Sigma_s}{4\pi} & 0 & 0 \\ 0 & 0 & 0 & \frac{\Sigma_s}{4\pi} & 0 \\ 0 & 0 & 0 & 0 & \frac{\Sigma_s}{4\pi} \end{bmatrix}_{p\times p} \tag{31b}$$

$$C_2 = \begin{bmatrix} \frac{\Sigma_a}{4\pi} & 0 & 0 & 0 & 0 \\ 0 & \frac{\Sigma_a}{4\pi} & 0 & 0 & 0 \\ 0 & 0 & \frac{\Sigma_a}{4\pi} & 0 & 0 \\ 0 & 0 & 0 & \frac{\Sigma_a}{4\pi} & 0 \\ 0 & 0 & 0 & 0 & \frac{\Sigma_a}{4\pi} \end{bmatrix}_{p\times p} \tag{31c}$$

$$E_1 = \begin{bmatrix} E_{p\times p} & 0_{p\times p^2} \end{bmatrix}_{p\times(p+p^2)} \tag{31d}$$

The presentation of the radial transverse leakage term matrix C_3 is provided later in Eq. (45). During the inner iteration, the 1D axial scalar flux errors are updated and the 2D radial scalar flux errors keep constant. The updated scalar flux is shown in Eq. (32a) and the next inner iteration is displayed as Eq. (32e):

$$D^{l+\frac{1}{2}} = \sum_{m=1}^{M} w_m YY_m B_m^{l+\frac{1}{2},n_1} = R_1^{n_1} S^l \tag{32a}$$

$$YY_m = \begin{bmatrix} \frac{1}{2} & \frac{1}{2} & 0 & 0 & 0 \\ 0 & \frac{1}{2} & \frac{1}{2} & 0 & 0 \\ \cdots & \cdots & \cdots & \cdots & \cdots \\ \frac{1}{2}e^{i\Sigma_t\lambda_z\Delta_z} & 0 & 0 & 0 & \frac{1}{2} \end{bmatrix}_{p\times p} \tag{32b}$$

$$S^{l+\frac{1}{2},n_1} = \begin{bmatrix} R_1^{n_1} \\ E_3 \end{bmatrix} S^l = RR_1^{n_1} S^l \tag{32c}$$

$$E_3 = \begin{bmatrix} 0_{p^2\times p} & E_{p^2\times p^2} \end{bmatrix}_{p^2\times(p+p^2)} \tag{32d}$$

$$B_m^{l+\frac{1}{2},n_1+1} = Y_m^{-1}\left(C_1E_1RR_1^{n_1} + C_2E_1 + C_3\right)S^l \tag{32e}$$

Here, the presentations of $R_1^{n_1}$ and $RR_1^{n_1}$ depend on the n_1, when $n_1 = 1$:

$$R_1^1 = \sum_{m=1}^{M} w_m YY_m Y_m^{-1}(C_1E_1 + C_2E_1 + C_3) \tag{33a}$$

$$RR_1^1 = \begin{bmatrix} R_1^1 \\ E_3 \end{bmatrix} \tag{33b}$$

When $n_1 > 1$

$$R_1^{n_1} = \sum_{m=1}^{M} w_m Y Y_m Y_m^{-1}\left(C_1 E_1 R R_1^{n_1-1} + C_2 E_1 + C_3\right) \tag{33c}$$

$$R R_1^{n_1} = \begin{bmatrix} R_1^{n_1} \\ E_3 \end{bmatrix} \tag{33d}$$

After N_1 times inner iterations of the first 1D calculation, the axial transverse leakage for the 2D calculation is obtained using Eq. (1b). According to the periodic boundary condition, the top boundary net current error term can be calculated by the bottom boundary net current error term, which is shown in Eq. (34a). The axial transverse leakage error term is shown in Eq. (34b):

$$\begin{aligned} G_{I,J,K-\frac{1}{2}}^{l+\frac{1}{2}} &= \sum_{m=1}^{M} w_m \mu_m B_{m,I,J,0}^{l+\frac{1}{2},N_1} \\ &= \sum_{m=1}^{M} w_m \mu_m Y_m^{-1}\left(C_1 E_1 R R_1^{N_1-1} + C_2 E_1 + C_3\right) S^l \end{aligned} \tag{34a}$$

$$TL_{axial} = \frac{1}{4\pi\Delta_z}\left(\tilde{J}_{I,J,K}^{top} - \tilde{J}_{I,J,K}^{bottom}\right) = \frac{e^{i\Sigma_t\lambda_z\Delta_z} - 1}{4\pi\Delta_z} G_{I,J,K-\frac{1}{2}}^{l+\frac{1}{2}} = P_1 S^l \tag{34b}$$

Then the Fourier ansatz is applied into the 2D linearized Eq. (23). The intermediate fine mesh boundary angular flux of 2D SN is calculated as:

$$A_{m,i\pm\frac{1}{2},j\pm\frac{1}{2},K}^{l+\frac{1}{2},n_2+1} = X_m^{-1}\left(\frac{\Sigma_s}{4\pi} E_4 E_3 S^{l,n_2} + \frac{\Sigma_a}{4\pi} E_4 E_3 S^l - E_4 P_1 S^l\right) \tag{35}$$

Where X_m is the matrix of the 2D SN transport calculation with size of $p^2 \times p^2$, E_4 is a transform matrix that converts the matrix with size of p^2 into matrix with size of $2p^2$. Defining the 2D radial fine-mesh boundary angular flux error matrix $A_{m,i\pm\frac{1}{2},j\pm\frac{1}{2},K}^{l+\frac{1}{2},n_2+1}$, the notation of the 2D mesh is shown in Fig. 3. It contains $2p^2$ fine mesh edge angular flux that ordered from bottom to top.

The detailed presentations of the matrices are:

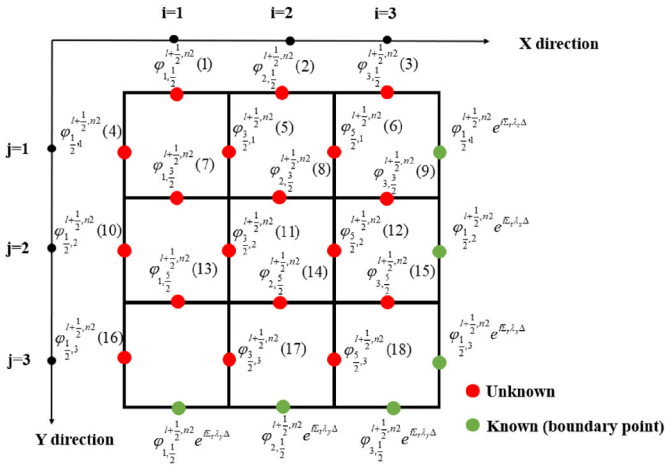

Fig. 3. Mesh notation of the 2D calculation.

$$A_{m,i\pm\frac{1}{2},j\pm\frac{1}{2},K}^{l+\frac{1}{2},n_2} = \begin{bmatrix} \tilde{\phi}_{m,1,\frac{1}{2}}^{l+\frac{1}{2},n_2} \\ \cdots \\ \tilde{\phi}_{m,p,\frac{1}{2}}^{l+\frac{1}{2},n_2} \\ \vdots \\ \tilde{\phi}_{m,\frac{1}{2},p}^{l+\frac{1}{2},n_2} \\ \cdots \\ \tilde{\phi}_{m,\frac{2p-1}{2},p}^{l+\frac{1}{2},n_2} \\ \vdots \end{bmatrix}_{2p^2\times 1} \tag{36b}$$

$$E_4 = \left[E_{p^2\times p^2}; 0_{p^2\times p^2}\right]_{2p^2\times p^2} \tag{36c}$$

During the inner iteration, the 2D radial scalar flux errors and the scattering source error are updated. The 1D axial scalar flux errors, the absorption term and the axial transverse leakage error term keep constant. The updated scalar flux is presented in Eq. (37a) and the following inner iteration is presented in Eq. (37d):

$$X_m = \begin{bmatrix} \frac{-\eta_m}{h_1} + \frac{\Sigma_t}{4} & [0\cdots 0]_{p-1} & \frac{-\xi_m}{h_1} + \frac{\Sigma_t}{4} & \frac{\xi_m}{h_1} + \frac{\Sigma_t}{4} & [0\cdots 0]_{p-2} & \frac{\eta_m}{h_1} + \frac{\Sigma_t}{4} & \cdots & [0\cdots 0] \\ 0 & \frac{-\eta_m}{h_1} + \frac{\Sigma_t}{4} & [0\cdots 0]_{p-1} & \frac{-\xi_m}{h_1} + \frac{\Sigma_t}{4} & \frac{\xi_m}{h_1} + \frac{\Sigma_t}{4} & [0\cdots 0]_{p-2} & \frac{\eta_m}{h_1} + \frac{\Sigma_t}{4} & [0\cdots 0] \\ \vdots & \vdots & \vdots & \vdots & \vdots & \vdots & \vdots & \vdots \\ 1 & [0\cdots 0]_{p-1} & -1 & -1 & [0\cdots 0]_{p-2} & 1 & \cdots & [0\cdots 0] \\ 0 & 1 & [0\cdots 0]_{p-1} & -1 & -1 & [0\cdots 0]_{p-2} & 1 & [0\cdots 0] \\ \vdots & \vdots & \vdots & \vdots & \vdots & \vdots & \vdots & \vdots \end{bmatrix}_{2p^2\times 2p^2} \tag{36a}$$

$$C^{l+\frac{1}{2}} = \sum_{m=1}^{M} w_m XX_m A_m^{l+\frac{1}{2},n_2} = R_2^{n_2} S^l \tag{37a}$$

$$XX_m = \begin{bmatrix} \frac{1}{4} & [0\cdots0]_{p-1} & \frac{1}{4} & \frac{1}{4} & [0\cdots0]_{p-2} & \frac{1}{4} & \cdots & [0\cdots0] \\ 0 & \frac{1}{4} & [0\cdots0]_{p-1} & \frac{1}{4} & \frac{1}{4} & [0\cdots0]_{p-2} & \frac{1}{4} & [0\cdots0] \\ \vdots & \vdots & \vdots & \vdots & \vdots & \vdots & \vdots & \vdots \end{bmatrix}_{p^2\times 2p^2} \tag{37b}$$

$$S^{l+\frac{1}{2},n_2} = \begin{bmatrix} E_1 \\ R_2^{n_2} \end{bmatrix} S^l = RR_2^{n_2} S^l \tag{37c}$$

$$A_{m,i\pm\frac{1}{2},j\pm\frac{1}{2},K}^{l+\frac{1}{2},n_2+1} = X_m^{-1}\left(\frac{\Sigma_s}{4\pi}E_4E_3RR_2^{n_2} + \frac{\Sigma_a}{4\pi}E_4E_3 - E_4P_1\right)S^l \tag{37d}$$

Here, the presentations of $R_2^{n_2}$ and $RR_2^{n_2}$ depend on the n_2, when $n_2 = 1$:

$$R_2^1 = \sum_{m=1}^{M} w_m XX_m X_m^{-1}\left(\frac{\Sigma_s}{4\pi}E_4E_3 + \frac{\Sigma_a}{4\pi}E_4E_3 - E_4P_1\right) \tag{40a}$$

$$RR_2^1 = \begin{bmatrix} E_1 \\ R_2^1 \end{bmatrix} \tag{40b}$$

When $n_2 > 1$:

$$R_2^{n_2} = \sum_{m=1}^{M} w_m XX_m X_m^{-1}\left(\frac{\Sigma_s}{4\pi}E_4E_3RR_2^{n_2-1} + \frac{\Sigma_a}{4\pi}E_4E_3 - E_4P_1\right) \tag{40c}$$

$$RR_2^{n_2} = \begin{bmatrix} E_1 \\ R_2^{n_2} \end{bmatrix} \tag{40d}$$

After N_2 2D SN inner iterations, the radial boundary net current can be obtained by accumulating the edge angular flux. The left boundary net current is presented as Eq. (41a) and the behind boundary net current is presented as Eq. (41b).

$$G_{I-\frac{1}{2}J,K}^{l+\frac{1}{2}} = \frac{1}{p}\sum_{j=1}^{p}\sum_{m=1}^{M} w_m\xi_m A_{m,\frac{1}{2}j,K}^{l+\frac{1}{2},N_2} = \frac{1}{p}\sum_{j=1}^{p}\sum_{m=1}^{M} w_m\xi_m X_m^{-1}\left(\frac{\Sigma_s}{4\pi}E_4E_3RR_2^{N_2-1} + \frac{\Sigma_a}{4\pi}E_4E_3 - E_4P_1\right)S^l \tag{41a}$$

$$G_{IJ-\frac{1}{2},K}^{l+\frac{1}{2}} = \frac{1}{p}\sum_{i=1}^{p}\sum_{m=1}^{M} w_m\eta_m A_{m,i,\frac{1}{2}K}^{l+\frac{1}{2},N_2} = \frac{1}{p}\sum_{i=1}^{p}\sum_{m=1}^{M} w_m\eta_m X_m^{-1}\left(\frac{\Sigma_s}{4\pi}E_4E_3RR_2^{N_2-1} + \frac{\Sigma_a}{4\pi}E_4E_3 - E_4P_1\right)S^l \tag{41b}$$

The right boundary and the front boundary net current are presented by the left boundary and behind boundary net current according to the periodic boundary condition, which is:

$$G_{I+\frac{1}{2}J,K}^{l+\frac{1}{2}} = G_{I-\frac{1}{2}J,K}^{l+\frac{1}{2}} e^{i\Sigma_t\lambda_x\Delta} \tag{42a}$$

$$G_{IJ+\frac{1}{2},K}^{l+\frac{1}{2}} = G_{IJ-\frac{1}{2},K}^{l+\frac{1}{2}} e^{i\Sigma_t\lambda_y\Delta} \tag{42b}$$

Therefore, the radial transverse leakage term for the second 1D SN calculation can be obtained:

$$\frac{1}{4\pi\Delta}\left(\tilde{J}_{IJ,K}^{x_R} - \tilde{J}_{IJ,K}^{x_L} + \tilde{J}_{IJ,K}^{y_R} - \tilde{J}_{IJ,K}^{y_L}\right) = \frac{e^{i\Sigma_t\lambda_x\Delta}-1}{4\pi\Delta}G_{I-\frac{1}{2}J,K}^{l+\frac{1}{2}} + \frac{e^{i\Sigma_t\lambda_y\Delta}-1}{4\pi\Delta}G_{IJ-\frac{1}{2},K}^{l+\frac{1}{2}} = P_2S^l \tag{43}$$

The intermediate matrix is defined as follows:

$$L_1 = \frac{1}{p}\begin{bmatrix} \frac{\eta_m}{\Delta}\left(e^{i\Sigma_t\lambda_y\Delta}-1\right)\left(\underbrace{1,\cdots1}_{p},0,0,\cdots\right), \frac{\xi_m}{\Delta}\left(e^{i\Sigma_t\lambda_x\Delta}-1\right)\left(\underset{p}{0},1,\underset{p}{0},1,\cdots\right) \\ \vdots \end{bmatrix}_{p\times 2p^2} \tag{44a}$$

$$L_2 = \begin{bmatrix} \frac{\mu_m}{\Delta_z}\left(e^{i\Sigma_t\lambda_z\Delta_z}-1\right)\left(1,\ \underset{p-1}{0}\right) \\ \vdots \\ \left(\underbrace{0,\cdots,0}_{p}\right) \\ \vdots \end{bmatrix}_{2p^2\times p} \tag{44b}$$

Similar as the presentation of P_2, the radial transverse leakage term for the first 1D calculation C_3 can be presented as follows:

$$C_3 = \left(\frac{e^{i\Sigma_t\lambda_x\Delta}-1}{4\pi\Delta p}\sum_{j=1}^{p}\sum_{m=1}^{M} w_m\xi_m + \frac{e^{i\Sigma_t\lambda_y\Delta}-1}{4\pi\Delta p}\sum_{i=1}^{p}\sum_{m=1}^{M} w_m\eta_m\right) \times \left(\frac{\Sigma_t}{4\pi}\begin{bmatrix} Y_m & L_1 \\ X_m & L_2 \end{bmatrix}^{-1}\begin{bmatrix} E_{(p+p^2)\times(p+p^2)} \\ 0_{p^2\times(p+p^2)} \end{bmatrix}\right) \tag{45}$$

After N_1 times 1D axial SN calculation and N_2 times 2D radial SN calculation, the intermediate scalar flux error term is presented as:

$$S^{l+\frac{1}{2}} = \begin{bmatrix} R_1^{N_1} \\ R_2^{N_2} \end{bmatrix} S^l = TS^l \tag{46}$$

The radial angular flux Eq. (43) is substituted into the second 1D SN calculation Eq. (19b). The form of the second 1D SN calculation is similar as the first 1D SN calculation and it is shown in Eq. (47):

$$B_{m,I,J,k\pm\frac{1}{2}}^{l+\frac{1}{2},n_3+1} = Y_m^{-1}\left(C_1E_1TS^{l,n_3} + C_2E_1TS^l - P_2S^l\right) \tag{47}$$

Same as the first 1D SN calculation, during inner iteration, the scattering error term is updated, while, the fission source and the radial transverse leakage is fixed. The updated scalar flux and the next inner iteration are presented as:

$$D^{l+\frac{1}{2}} = \sum_{m=1}^{M} w_m Y Y_m B_m^{l+\frac{1}{2},n_3} = R_3^{n_3}S^l \tag{48a}$$

$$S^{l+\frac{1}{2},n_3} = \begin{bmatrix} R_3^{n_3} \\ E_3 \end{bmatrix} S^l = RR_3^{n_3}S^l \tag{48b}$$

$$B_m^{l+\frac{1}{2},n_3+1} = Y_m^{-1}\left(C_1E_1RR_3^{n_3}T + C_2E_1T - P_2\right)S^l \tag{48c}$$

Here, the presentations of $R_3^{n_3}$ and $RR_3^{n_3}$ depend on the n_3, when $n_3 = 1$:

$$R_3^1 = \sum_{m=1}^{M} w_m Y Y_m Y_m^{-1}(C_1E_1T + C_2E_1T - P_2) \tag{49a}$$

$$RR_3^1 = \begin{bmatrix} R_3^1 \\ E_3 \end{bmatrix} \tag{49b}$$

When $n_3 > 1$

$$R_3^{n_3} = \sum_{m=1}^{M} w_m Y Y_m Y_m^{-1}\left(C_1E_1RR_3^{n_3-1}T + C_2E_1T - P_2\right) \tag{49c}$$

$$RR_3^{n_3} = \begin{bmatrix} R_3^{n_3} \\ E_3 \end{bmatrix} \tag{49d}$$

Then a newly updated axial boundary net current is obtained by accumulating the boundary angular flux, which is:

$$\begin{aligned} G_{I,J,K-\frac{1}{2}}^{l+\frac{1}{2}} &= \sum_{m=1}^{M} w_m\mu_m B_{m,I,J,0}^{l+\frac{1}{2},N_3} \\ &= \sum_{m=1}^{M} w_m\mu_m Y_m^{-1}\left(C_1E_1RR_3^{N_3-1}T + C_2E_1T - P_2\right)S^l \end{aligned} \tag{50}$$

The updated scalar flux error matrix is shown:

$$S^{l+\frac{1}{2}} = \begin{bmatrix} R_3^{N_3} \\ R_2^{N_2} \end{bmatrix} S^l = T_2S^l \tag{51}$$

After the 1D axial SN calculation and the 2D radial calculation, six net currents $G_{I\pm\frac{1}{2},J\pm\frac{1}{2},K\pm\frac{1}{2}}^{l+\frac{1}{2}}$ are supplied to 3D CMFD Eq. (25).

$$\begin{aligned} &E^{l+\frac{1}{2}}\left\{\frac{\Delta_z}{\Delta}\left[\left(e^{i\Sigma_t\lambda_x\Delta}+e^{-i\Sigma_t\lambda_x\Delta}+e^{i\Sigma_t\lambda_y\Delta}+e^{-i\Sigma_t\lambda_y\Delta}-4\right)+\frac{\Delta}{\Delta_z}\left(e^{i\Sigma_t\lambda_z\Delta_z}+e^{-i\Sigma_t\lambda_z\Delta_z}-2\right)\right]\right\} \\ &\quad+\left[\frac{\Delta_z}{D_{od}}\left(e^{i\Sigma_t\lambda_x\Delta}-1\right)G_{I-\frac{1}{2},J,K}^{l+\frac{1}{2}}+\frac{\Delta_z}{D_{od}}\left(e^{i\Sigma_t\lambda_y\Delta}-1\right)G_{I,J-\frac{1}{2},K}^{l+\frac{1}{2}}+\frac{\Delta}{D_{od}}\left(e^{i\Sigma_t\lambda_z\Delta_z}-1\right)G_{I,J,K-\frac{1}{2}}^{l+\frac{1}{2}}\right]S^l \\ &\quad=F^{l+1}\left\{\frac{\Delta_z}{\Delta}\left[\left(e^{i\Sigma_t\lambda_x\Delta}+e^{-i\Sigma_t\lambda_x\Delta}+e^{i\Sigma_t\lambda_y\Delta}+e^{-i\Sigma_t\lambda_y\Delta}-4\right)+\frac{\Delta}{\Delta_z}\left(e^{i\Sigma_t\lambda_z\Delta_z}+e^{-i\Sigma_t\lambda_z\Delta_z}-2\right)\right]\right\} \end{aligned} \tag{52}$$

Table 1
Test problem specifications.

$\Sigma_t(cm^{-1})$	$\nu\Sigma_f(cm^{-1})$	$\Sigma_s(cm^{-1})$	p	Quadrature set	$\Delta_z(cm)$	$\Delta(cm)$	Order of DGFEM
1.0	0.01	0.9	2	S6-Gaussian Legendre	1.0–10.0	1.0	2

Table 2
Outer iterations for 3X3 partially lattice problem (Axial 36 layer).

Case	Number of 1st 1D sweeping	Number of 2D sweeping	Number of 2nd 1D sweeping	Keff	Number of outer iterations
Reference	–	–	–	1.21566±0.00028	–
1	1	1	1	1.21597	30
2	2	1	1	1.21597	29
3	5	1	1	1.21597	27
4	5	1	5	1.21597	25
5	5	2	5	1.21597	23
6	5	5	5	1.21597	20
7	5	2	0	1.21597	36
8	5	2	2	1.21597	25

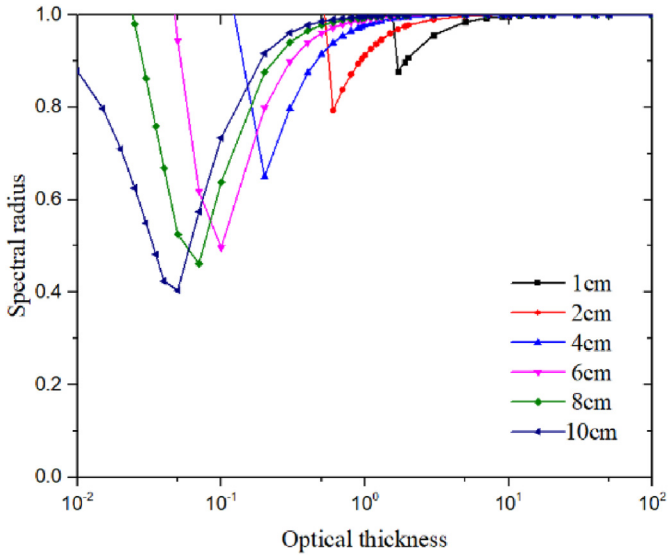

Fig. 4. Spectral radius of different axial mesh size.

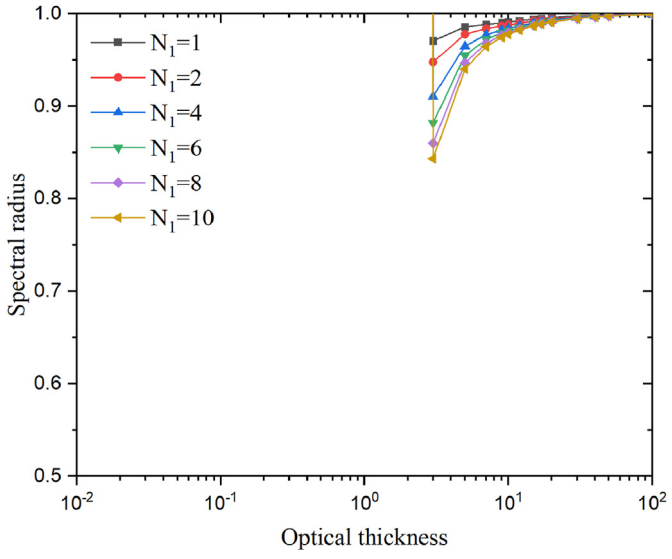

Fig. 5. Spectral radius of different N_1.

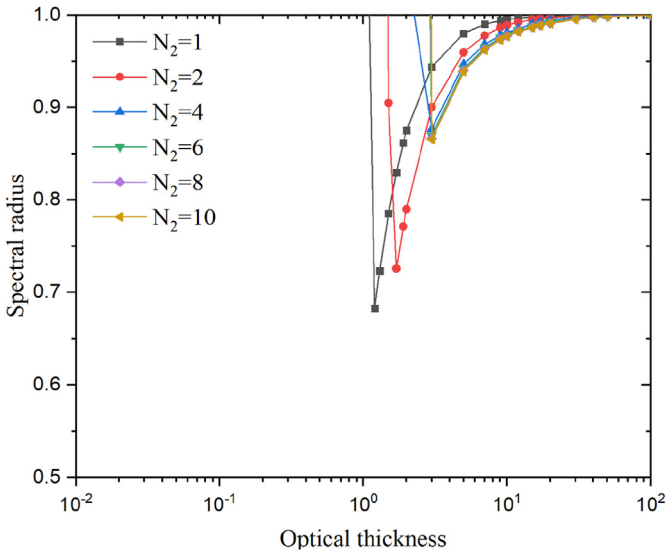

Fig. 6. Spectral radius of different N_2.

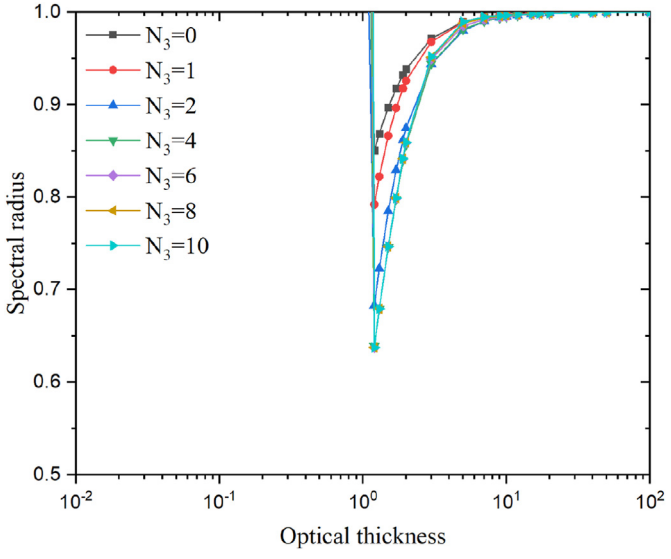

Fig. 7. The influence of two times 1D axial SN calculation per outer iteration.

From Eq. (52), it can be derived that:

$$\delta = F^{l+1} - E^{l+\frac{1}{2}} = \frac{\left[\Delta_z\left(e^{i\Sigma_t\lambda_x\Delta}-1\right)G^{l+\frac{1}{2}}_{I-\frac{1}{2},J,K} + \Delta_z\left(e^{i\Sigma_t\lambda_y\Delta}-1\right)G^{l+\frac{1}{2}}_{I,J-\frac{1}{2},K} + \Delta\left(e^{i\Sigma_t\lambda_z\Delta_z}-1\right)G^{l+\frac{1}{2}}_{I,J,K-\frac{1}{2}}\right]}{D_{ad}\frac{\Delta_z}{\Delta}\left(e^{i\Sigma_t\lambda_x\Delta}+e^{-i\Sigma_t\lambda_x\Delta}+e^{i\Sigma_t\lambda_y\Delta}+e^{-i\Sigma_t\lambda_y\Delta}-4\right)+D_{ad}\frac{\Delta}{\Delta_z}\left(e^{i\Sigma_t\lambda_z\Delta_z}+e^{-i\Sigma_t\lambda_z\Delta_z}-2\right)}S^l \tag{53}$$

The fine-mesh scalar fluxes are updated by the coarse mesh scalar flux as Eq. (26), the final fine-mesh error transition matrix is shown:

$$S^{l+1} = T_2S^l + \delta = T_3S^l \tag{54}$$

Where T_3 is the final error transition matrix of the whole calculation process. The spectral radius is the maximum eigenvalue of the error transition matrix for all the combinations of Fourier frequencies [23,24]:

$$\rho = \max\left(w\left(\lambda_x,\lambda_y,\lambda_z\right)\right) = \max\left(\max\left(abs\left(eig\left(T_3\right)\right)\right),\forall\lambda_x,\lambda_y,\lambda_z\right) \tag{55}$$

The Fourier frequency $\lambda_x,\lambda_y,\lambda_z$ are shown in Eq. (54). L_x, L_y, L_z is the domain size of the problem in X, Y, Z direction.

$$\lambda_x = \frac{2\pi i}{\Sigma_t L_x}, \mathrm{i} = 1,2,\cdots I-1, I = \frac{L_x}{\Delta} \tag{56a}$$

$$\lambda_y = \frac{2\pi j}{\Sigma_t L_y}, j = 1,2,\cdots J-1, J = \frac{L_y}{\Delta} \tag{56b}$$

$$\lambda_z = \frac{2\pi k}{\Sigma_t L_z}, k = 1,2,\cdots K-1, K = \frac{L_z}{\Delta_z} \tag{56c}$$

5. Results and discussion

The convergence performance of traditional 2D/1D coupling method for solving neutron transport k-eigenvalue problem is discussed here. The computational domain here is a homogeneous cube model with the size of $10cm \times 10cm \times (10 \sim 100)cm$ and periodic boundary conditions. The computational parameters are listed in Table 1.

5.1. Divergence problem in small axial mesh size

In this part, the divergence problem of 2D/1D coupling method is shown and analyzed. Here, set the number of inner iterations of 1D calculation(N_1/N_3) as 2 and the number of inner iterations of 2D calculation (N_2) as 1. For other combinations of the inner iterations, the phenomenon is similar. Keeping the radial mesh size as a constant as 1.0 cm, the axial mesh size changes from 1.0 to 10.0 cm. The convergence behavior of different axial mesh size is shown in Fig. 4. When the axial mesh size is 10.0 cm, the 2D/1D coupling method converge in all the optical thickness region. However, when finer the axial mesh size, the 2D/1D method diverge in small optical thickness region. Moreover, with the decrease of the axial mesh size, the divergence problem become more and more serious. In practice, utilizing the fine axial mesh size can improve the accuracy but it may lead to the divergence of the 2D/1D coupling method [10,11]. The Fourier analysis results show the divergence phenomenon in small axial mesh size. In section 5.2, several attempts are tried to solve the divergence problem in small axial mesh size. Therefore, the axial mesh size is set as 1.0 cm in the next section.

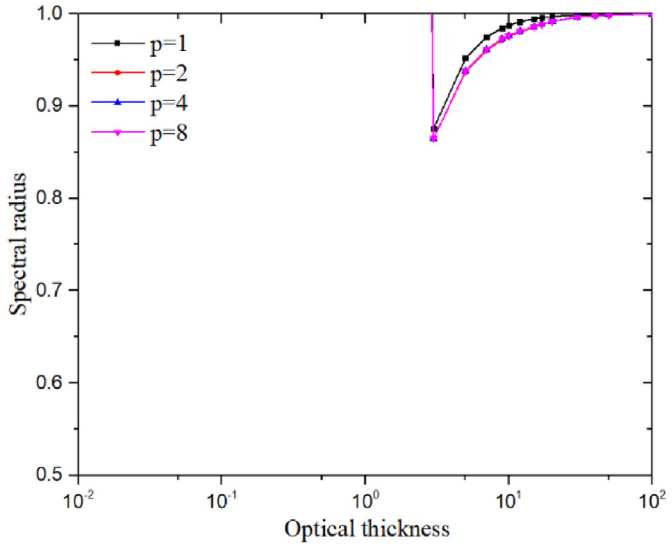

Fig. 8. The influence of p on the spectral radius for traditional scheme.

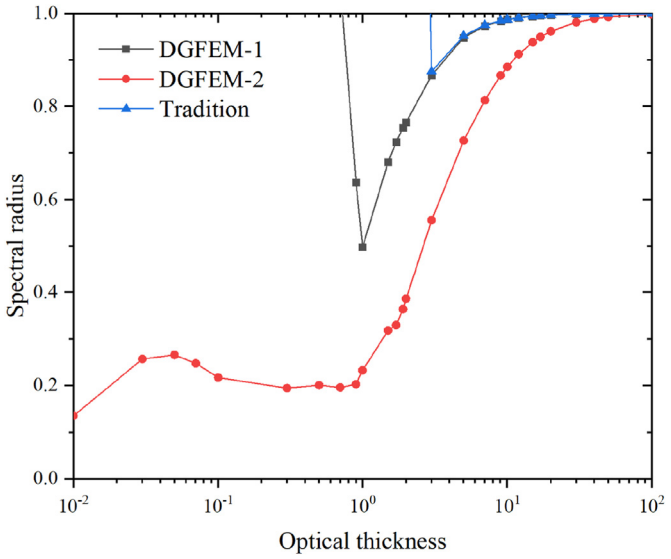

Fig. 9. The influence of 1D axial SN solver on the spectral radius.

5.2. Common attempts for solving the divergence problem

Empirically evidence suggests that more than one inner iteration can supply a tight convergence. Therefore, a common attempt for solving the divergence problem is that changing the number of inner iterations of 2D or 1D calculation. Firstly, by keeping N_2 and N_3 as constant and changing N_1, the convergence behavior is shown in Fig. 5. N_2 is set as 6, N_3 is set as 1, other combinations of N_2 and N_3 achieve the similar results. It can be clearly seen that the increase of N_1 achieves better convergence rate. Also, with the increase of the N_1, the decrement of the spectral radius slackens. It is noted that the increase of the 1D SN calculation cannot solve the divergence problem. For optical thickness between 10^{-2} to 1, all the strategies fail.

Secondly, the effect of inner iterations number of 2D calculation is analyzed. Here, N_1 is set as 6 and N_3 is set as 2, other combinations of N_1 and N_3 achieve the similar trend. The results are shown in Fig. 6. It can be seen in the figure that when N_2 is larger than 4, the curves tend to be consistence. In small optical thickness around 10^{-2} to 10^{0}, all the iteration strategies diverge. When N_2 is set as 1, the 2D/1D method converge in optical thickness region between 1 and 3. However, the increase of N_2 lead to the divergence in this optical thickness region. On the other side, the increase of N_2 do benefit to the spectral radius for high optical thickness region. The smallest spectral radius for $N_2 = 2$ is around 0.7 and for $N_2 > 4$ is around 0.85. In all, the change of N_2 cannot solve the divergence problem in small axial mesh size.

In practice, two 1D axial SN calculations per outer iteration, as shown in Fig. 1, can improve the convergence rate. The influence of two 1D axial SN calculations on the spectral radius is shown in Fig. 7. Here N_1 and N_2 are set as 6 and1 to clearly present the result. As a comparison, the other strategy is applied, which the second 1D axial SN calculation is deleted and is labeled as $N_3 = 0$ in the figure. In this strategy, the fine-mesh scalar flux error transition matrix is shown in Eq. (46), and the axial net current for 3D CMFD is calculated from the first 1D axial SN calculation as shown in Eq. (34). The results show that the usage of two 1D axial SN calculations per outer iteration can reduce the spectral radius of the system. With the increase of the N_3, the acceleration effect is more obvious. However, the usage of two 1D axial SN calculations cannot solve the divergence problem in small optical thickness region.

It can be seen from Figs. 5 to 7 that for small optical thickness region from 10^{-2} to 10^{0}, all the combinations among N_1, N_2, N_3 diverge. The change the number of inner iterations and the usage of two 1D SN calculations per outer iteration cannot solve the divergence problem.

5.3. The influence of the 1D axial SN solver

The 1D axial SN solver plays an important role in the 2D/1D coupling method. A comparison between the traditional axial 1D SN based 2D/1D coupling method (traditional scheme) and 1D axial DGFEM SN based 2D/1D coupling method (DGFEM scheme) is made here. The calculation flow of DGFEM scheme is the same as the traditional scheme, the only difference is that it adopts DGFEM SN as 1D axial solver. Different from the traditional SN FDM, DGFEM introduced the spatial basis functions to represent the solutions within each mesh. Here, the axial DGFEM SN mesh size is the same as the CMFD coarse mesh size. The detailed theory of the DGFEM SN is shown in Ref. [20].

The errors of DGFEM scheme contains two parts, which are the different orders of scalar flux moments in axial direction and the 2D radial fine mesh scalar flux. Instead of the axial fine-mesh scalar flux errors in traditional scheme, the DGFEM scheme contains (order+1) number of axial flux moment errors. The Fourier analysis of the DGFEM scheme is similar as the Fourier analysis of the traditional scheme here shown in Section 4. The detailed linearization and the Fourier analysis process of DGFEM scheme is shown in the previous work [28]. Different from the previous work, here two times 1D DGFEM SN calculation are applied here. The disposal of the 2-nd time 1D calculation, especially the presentation of the radial transverse leakage term from the 2D radial calculation is the same as the traditional scheme as shown in Eq. (45)- Eq. (51).

Two kinds of DGFEM schemes tested here, which labeled as DGFEM-1 and DGFEM-2. It is worth noted that the 0-th order scalar flux moment is the coarse-mesh scalar flux in DGFEM scheme. In DGFEM-1 scheme, this 0-th order scalar flux moment in the scattering source term is updated during the 1D SN calculation. In DGFEM-2 scheme, this 0-th order scalar flux moment in the scattering source term is fixed. In both two DGFEM schemes, the 0-th order scalar flux moment in the fission source term is fixed.

Here, the number of the 1st time1D inner sweeping, the number of the 2D inner sweeping and the number of the 2nd time 1D inner sweeping are set as 6, 6 and 2, respectively. For DGFEM scheme, the axial SN mesh size is the same as the coarse mesh size, which means the number of fine mesh per coarse mesh (p) is 1 in axial

Table 3
DGFEM-2 scheme calculation results for 108/216 axial layer.

Case	Keff	Number of outer iterations
108 axial layers	1.21578	31
216 axial layers	1.21578	43

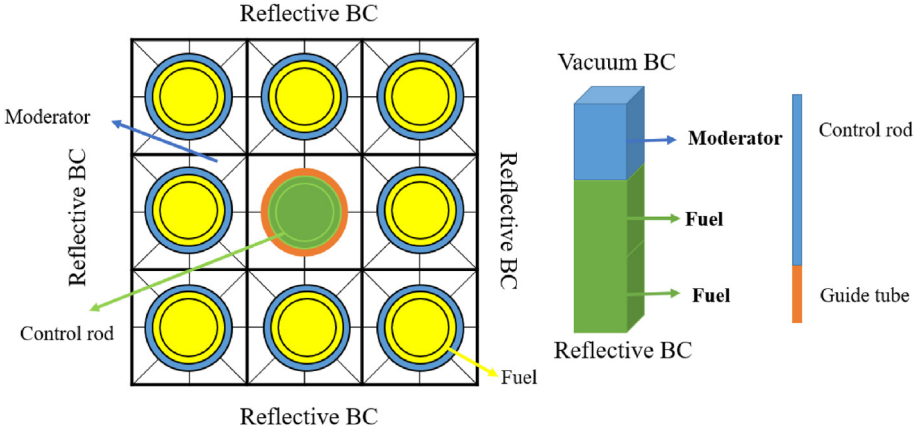

Fig. 10. The geometry of 3X3 partially rodded lattice problem.

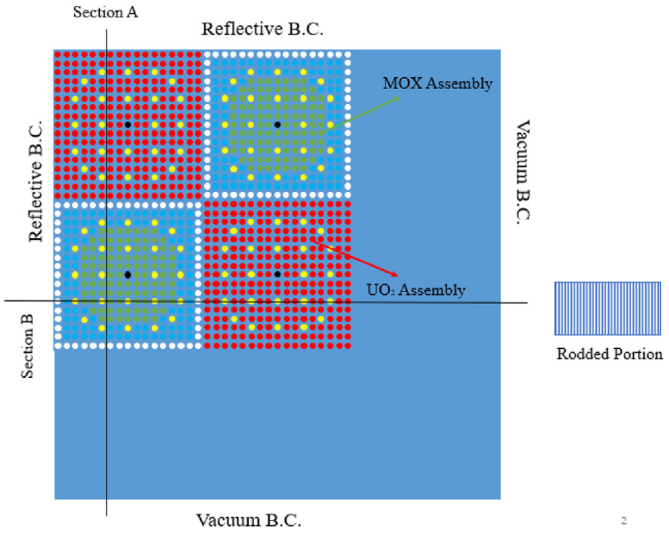

Fig. 11. The geometry of C5G7 benchmark.

direction. However, to obtain the enough accuracy, for traditional scheme, p is often higher than 1 in axial direction. For traditional scheme, the influence of axial p on the spectral radius is shown in Fig. 8.

It can be seen in Fig. 8 that the value of p has slightly influence on the spectral radius. To make a comparison with DGFEM scheme, in the traditional scheme, p is set as 1 in axial direction.

The influence of the 1D axial SN solver on the spectral radius is shown in Fig. 9. It can be seen clearly that the traditional scheme and DGFEM scheme without fixed 0-th order scalar flux moment (DGFEM-1) diverge in small optical thickness region between 10^{-2} to 10^{0}. The DGFEM scheme with fixed 0-th order scalar flux moment (DGFEM-2) solve this problem. For DGFEM-1, the 0-th order scalar flux moment in the scattering source term is updated during 1D axial SN calculation. For DGFEM-2, the 0-th order scalar flux moment in the scattering source term keeps constant during the 1D axial SN calculation, which means the updated 0-th order scalar flux moment is abandoned. Then after the 2D radial calculation, the 0-th order scalar flux moment is updated by the coarse-mesh scalar flux calculated from 2D radial calculation.

A reasonable explanation for the divergence problem in small optical thickness region for traditional scheme is that in Eq. (11), the right side of the iteration contains negative elements. The right side of Eq. (11) contains the scattering source term, fission source term and the radial transverse leakage term. The expression of the radial transverse leakage term is shown in Eq. (45). Detailed formula of the term L_2 in Eq. (45) is shown in Eq. (44b). When the axial mesh size Δ_z is small, the item $\frac{\mu_m}{\Delta_z}(e^{i\Sigma_t\lambda_z\Delta_z}-1)$ in L_2 maybe a huge negative value and lead to the negative radial transverse leakage term. In this case, the total source of Eq. (11) is probably negative. Then the scalar flux and the axial net current calculated from 1D axial calculation diverge and lead to the divergence of 2D/1D coupling method. In DGFEM scheme, the high order equations contain no transverse leakage moment so that the total sources for high order equations are always positive. It means that the high-order flux moments converge in small optical thickness region. The zero-order equation contains the radial transverse leakage term moment. Especially in small optical thickness region, this term may lead to the total source to be negative and then lead to the divergence of 0-th order scalar flux moment. It also explains the divergence problem of DGFEM-1 in small optical thickness region. If keeping the 0-th order scalar flux moment constant during the 1D axial calculation like DGFEM-2, all the different-order flux moments converge. The axial net current is calculated by different-order flux moments in DGFEM scheme. Therefore, in this case, the axial net current supplied to 2D radial calculation is reasonable and promise the convergence of 2D/1D coupling method in small optical thickness region.

For traditional scheme, when axial p is set as 1, the axial fine mesh is the same size of the coarse mesh. Then, the axial scalar flux is kept constant during 1D axial calculation, and is updated through coarse-mesh scalar flux like what DGFEM-2 scheme does. A possible speculation is that in this case, the traditional scheme may solve the divergence problem in small optical thickness region. Unfortunately, this speculation fails. When the negative total source exists, the 1D traditional SN calculation process may have problems and results in the unreasonable angular flux. For traditional SN, the scalar flux and the boundary net current are calculated by the angular flux. Even though the scalar flux is fixed, the boundary net current that used to calculate the axial transverse leakage term as shown in Eq. (7b) maybe unreasonable. Then the unreasonable axial transverse leakage may lead to the divergence of the 2D/1D coupling method in small optical thickness region. Compared with the traditional scheme, DGFEM-2 promises the

Table 4
Outer iterations for 3D C5G7-UR benchmark.

Case	Number of 1st 1D sweeping	Number of 2D sweeping	Number of 2nd 1D sweeping	Number of outer iterations
1	1	1	1	47
2	5	1	1	41
3	10	1	1	36
4	10	1	10	29
5	10	2	10	25
6	10	5	10	22
7	10	2	0	38
8	10	2	5	28

Table 5
Calculation results comparisons for 3D C5G7 benchmark.

Case	DGFEM-2 scheme			Traditional scheme		
	Error of Keff [20]	Computation time/hours	No. Outer iteration	Error of Keff [20]	Computation time/hours	No. Outer iteration
UR	-1pcm	4.18	20	7pcm	5.09	25
RA	9pcm	4.46	21	1pcm	5.04	25
RB	3pcm	4.37	21	−14pcm	5.06	25

convergence of the axial net current in small optical thickness region.

In all, the traditional SN based 2D/1D coupling method meets the divergence problem in small optical thickness region. For DGFEM SN based 2D/1D coupling method, the divergence problem can be solved by keeping the 0-th order scalar flux moment fixed during 1D axial calculation and updating it after the 2D radial calculation.

6. Numerical tests

6.1. 3 × 3 partially rodded lattice problem

To further evaluate the performance of Fourier analysis, a 3X3 partially rodded lattice problem, designed by Jarrett [11], is utilized as shown in Fig. 10. In radial direction, a square of UO_2 fuel pins is arranged with a guide tube in the center. In axial direction, there are two fuel layers and one moderator layer. The thickness of each layer is 21.42 cm, and the control rod is inserted 42.84 cm from top to bottom. All the radial boundaries and bottom boundary are reflective, and the top boundary is vacuum. In Jarrett's work, it is found that the eigenvalue does not appear to converge with increasing axial refinement [11]. When there are more than 72 planes axially, it suffers from the divergence problem.

In this work, the ray spacing of 2D MOC is fixed as 0.01 cm S8 quadrature set is implemented for angle discretization. This benchmark is conducted by single processor. The convergence criteria of eigenvalue and the scalar flux are 10^{-6} and 10^{-5}. When the number of the axial plane is set as 36, the traditional SN based 2D/1D coupling method converge. The influence of the number of inner iterations on the convergence is analyzed, and the results are shown in Table 2. The reference eigenvalue is calculated by Monte Carlo code OpenMC [25]. It can be seen in case 1 to 3 that the increase of the number of 1st time 1D sweeping decrease the number of outer iterations from 30 to 27, indicating that the spectral radius is reduced which is consistent with the Fourier analysis. Compared among the case 4–6, it is concluded that with the increase of the number of 2D sweeping, the number of outer iterations decrease from 25 to 20, agreeing with the Fourier analysis. According to the results of case 5, 7 and 8, it could draw a conclusion that the application of two times 1D SN calculation per outer iteration can obviously reduce the spectral radius. The outer iteration in this case reduces from 36 to 23. In all the cases, the eigenvalue is the same, whose error is 31pcm error.

When the number of axial plane is set as 108 and 216, which means smaller axial mesh size, the DGFEM-1 scheme and the traditional SN based 2D/1D coupling method diverge. While, the DGFEM-2 scheme with fixed 0-th order scalar flux moment converge in this case. The results of DGFEM-2 scheme are shown in Table .3. When the size of axial mesh is smaller than 0.595 cm (108 layer), the eigenvalue has little difference. The error of the 2D/1D coupling method is 12 pcm, which is smaller than that under 36-layers. With the increase of axial plane, the number of outer iterations increases from 31 to 43. The results show that choice of axial solver is a key issue for the convergence of 2D/1D method, and 1D DGFEM based 2D/1D coupling method with fixed 0-th order scalar flux moment is able to solve the divergence problem in small axial mesh size.

6.2. 3D C5G7 benchmark

To promise the generality of the results, the 3D C5G7 benchmarks [26] are tested. The geometry of the C5G7 benchmark is shown in Fig. 11 [20]. The related geometric parameters and the cross-sections can be seen in the reference [27]. In axial direction, the size of the benchmark is 64.26 cm and is divided into 36 layers. The benchmark contains 51 lattices in radial direction and each lattice is subdivided into 5 rings and 16 sectors. This benchmark is conducted by 144 processors (36 for axial direction and 4 for radial direction), and the spatial decomposition parallel strategy is used. The convergence criteria of eigenvalue and the scalar flux are 10^{-6} and 10^{-5}.

Firstly, the influence of the inner iterations on the convergence are analyzed and shown in Table .4. The phenomenon of 3D C5G7 benchmark is similar as the 3 × 3 partially rodded problem. Compared among the case 1 to 3, it can be clearly seen that the increase of the 1st time 1D sweeping significantly decrease the number of outer iterations from 47 to 36, which is consistent with the Fourier analysis. Increasing the number of 2D sweeping can also decrease the spectral radius, where the number of outer iterations decreases from 29 to 22 for case 4–6. According to the results of the case 5,7 and 8, it can be concluded that the implementation of two times 1D SN calculation per outer iteration can reduce the spectral radius.

To further verify the convergence improvement by employing the DGFEM as 1D solver, a comparison between the DGFEM-2 scheme and the traditional scheme are made here. To promise the tight convergence, the number of inner iterations for the 1D calculation and the 2D calculation are set as 10 and 2 respectively. The calculation results of the 3D C5G7 benchmarks are shown in Table .5. It can be seen that the convergence behavior of the DGFEM-2 scheme is better than the traditional scheme. For UR case, the number of outer iterations for the traditional scheme is 25, whereas for the DGFEM-2 scheme is only 20. For RA and RB cases, the number of outer iterations for the DGFEM-2 scheme is also smaller than the traditional scheme, which decreases from 25 to 21. Also, the computation time of the DGFEM-2 scheme is also smaller than the traditional scheme, which is about 85% of the traditional scheme.

7. Conclusion

2D/1D coupling method is an important neutron transport method. However, 2D/1D coupling method often suffers from the divergence problem in small axial mesh size. To analyze the convergence problem, a Fourier analysis of traditional SN based 2D/1D coupling method for k-eigenvalue neutron transport problems is implemented in this work. Fourier analysis results theoretically show the divergence problem of 2D/1D coupling method. Several common attempts are tested to solve this problem. The influence of the 1D axial solver is also analyzed by comparing the traditional SN and DGFEM SN based 2D/1D coupling method. The detailed conclusions are shown.

1. 2D/1D coupling method meets the divergence problem in small axial mesh size. When refining the axial mesh size, the 2D/1D coupling method may diverge in the thin optical thickness region.
2. The increase of the 1D axial SN inner iteration can reduce the spectral radius. However, with the increase of the number of inner iterations, the decrement of the spectral radius slackens, and the coupling method still suffers from divergence in the thin optical thickness region.
3. Increasing the number of 2D radial SN inner iteration do harm to the spectral radius in the small optical thickness region between 1 and 3. But it is benefit to the optical thickness region higher than 3. When the number of 2D radial SN inner iteration is higher than 4, the increase of the iteration has little impact on the spectral radius. The divergence problem in small optical

thickness region cannot be solved by changing the number of inner iterations.

4. Two times 1D axial calculation per outer iteration can reduce the spectral radius. The increment of the second 1D axial SN inner iteration can reduce the spectral radius and when the inner iteration is higher than 4, the curves tend to be consistent. However, the method still cannot solve the divergence problem in small optical thickness region.
5. The 1D axial solver has great influence on the convergence. For traditional 1D SN based 2D/1D coupling method, when finer the axial mesh size, it meets the divergence problem in small optical thickness region. When applying DGFEM based SN as axial 1D solver with fixed 0-th order scalar flux moment, it converges in all the optical thickness region.

Declaration of competing interest

The authors declare that they have no known competing financial interests or personal relationships that could have appeared to influence the work reported in this paper.

References

[1] J.Y. Cho, H.G. Joo, K.S. Kim, S.Q. Zee, Three-dimensional heterogeneous whole core transport calculation employing planar MOC solutions, Trans. Am. Nucl. Soc. 87 (2002) 234–236.
[2] N.Z. Cho, G.S. Lee, C.J. Park, Refinement of the 2D/1D fusion method for 3D whole core transport calculation, Trans. Am. Nucl. Soc. 87 (2002) 417–420.
[3] H.G. Joo, J.Y. Cho, K.S. Kim, C.C. Lee, S.Q. Zee, Methods and Performance of a Three-Dimensional Whole Core Transport Code DeCART. Proc. PHYSPR, American Nuclear Society, CD-ROM, 2004, 2004, Chicago, April 25-29, 2004.
[4] G.S. Lee, N.Z. Cho, 2D/1D fusion method solutions of the three-dimensional transport OECD benchmark problems C5G7 MOX, Prog. Nucl. Energy 48 (2006) 410–423.
[5] J.Y. Cho, K.S. Kim, C.C. Lee, et al., Axial SPN and radial MOC coupled whole core transport calculation, J. Nucl. Sci. Technol. (Tokyo, Jpn.) 44 (2007) 1156–1171.
[6] Y. Jung, H.G. Joo, Decoupled Planar MOC Solution for Dynamic Group Constant Generation in Direct Three-Dimensional Core Calculations. Proc. M&C, vol. 44, Saratoga Springs, NY. USA., 2009. May 3-7.
[7] Q. Shen, Y. Wang, D. Jabaay, et al., Transient analysis of C5G7-TD benchmark with MPACT, Ann. Nucl. Energy 125 (2018) 107–120. MAR.).
[8] B. Wang, Z. Liu, J. Chen, et al., A modified predictor-corrector quasi-static method in NECP-X for reactor transient analysis based on the 2D/1D transport method, Prog. Nucl. Energy 108 (Sep) (2018) 122–135.
[9] J. Ma, C. Hao, L. Liu, et al., Perturbation theory-based whole-core eigenvalue sensitivity and uncertainty (SU) analysis via a 2D/1D transport code, Sci. Technol.Nucl. Install. 2020 (2020) 13. Article ID 9428580.
[10] B.W. Kelly, E.W. Larsen, 2D/1D Approximations to the 3D Neutron Transport Equation I: Theory. Proc. M&C, 2013, Sun Valley, ID, USA, 2013. May 5-9.
[11] M. Jarrett, B. Kochunas, et al., Progress in Characterizing 2D/1D Accuracy in MPACT. Proc. M&C, 2017. Jeju, Korea. April 16-20.
[12] S.G. Hong, K.S. Kim, J.S. Song, Fourier convergence analysis of the rebalance methods for discrete ordinates transport equations in eigenvalue problems, Nucl. Sci. Eng. 164 (1) (2010) 33–52.
[13] A. Zhu, M. Jarret, Y. Xu, B. Kochunas, E. Larsen, T. Downar, An optimally diffusive coarse mesh finite difference method to accelerate neutron transport calculations, Ann. Nucl. Energy 95 (2016) 116–124.
[14] B.W. Kelly, E.W. Larsen, A consistent 2D/1D approximation to the 3D neutron transport equation, Nucl. Eng. Des. 295 (2015) 598–614.
[15] K.P. Keady, E.W. Larsen, Stability of SN k-eigenvalue iterations using CMFD acceleration, in: Proc. Int. Conf. On Mathematics and Computation (M&C), Supercomputing in Nuclear Applications (SNA) and the Monte Carlo (MC) Method, American Nuclear society, Nashville, Tennessee, USA, 2015. April 19-23.
[16] Y. Chan, S. Xiao, Convergence study of variants of CMFD acceleration schemes for fixed source neutron transport problems in 2D cartesian geometry with Fourier analysis, Ann. Nucl. Energy 134 (2019) 273–283.
[17] Y. Chan, S. Xiao, Convergence study of CMFD and lpCMFD acceleration schemes for k-eigenvalue neutron transport problems in 2D cartesian geometry with Fourier analysis, Ann. Nucl. Energy 133 (2019) 327–337.
[18] L. Jain, Prabhakaran, et al., Convergence study of CMFD based acceleration schemes for multi-group transport calculations with fission source using Fourier analysis, Ann. Nucl. Energy 160 (2021) (2021), 108314.
[19] L. Jain, Karthikeyan, et al., Comparative studies of iterative methods for solving the optimally diffusive coarse mesh finite difference accelerated transport equation, Ann. Nucl. Energy 157 (2021) (2021), 108211.
[20] B. Kong, K. Zhu, H. Zhang, C. Hao, J. Guo, F. Li, A discontinuous Galerkin finite element method based axial SN for the 2D/1D transport method, Prog. Nucl. Energy 152 (2022), 104391. October.
[21] X. Zhou, Z. Liu, L. Cao, H. Wu, Convergence analysis for the CMFD accelerated 2D/1D neutron transport method based on Fourier analysis, Nucl. Sci. Eng. 17 (2022), 108982.
[22] Y. Chan, S. Xiao, A linear prolongation CMFD acceleration for two-dimensional discrete ordinate k-eigenvalue neutron transport calculation with pin-resolved mesh using discontinuous Galerkin finite element method, Ann. Nucl. Energy 154 (2021), 108103.
[23] D. Wang, S. Xiao, A linear prolongation approach to stabilizing CMFD, Nucl. Sci. Eng. 190 (1) (2018) 45–55.
[24] D. Wang, S. Xiao, Stabilizing CMFD with Linear Prolongation, PHYSOR, Cancun, Mexico, 2018. April 22-26.
[25] K. Paul, E. Nicholas, et al., OpenMC: a state-of-the-art Monte Carlo code for research and development, Ann. Nucl. Eng. 82 (2015) 90–97.
[26] J.J. Klingensmith, Y.Y. Azmy, J.C. Gehin, et al., Tort solutions to the three-dimensional MOX benchmark, 3D extension C5G7MOX, Prog. Nucl. Energy 48 (5) (2006) 445–455.
[27] M.A. Smith, et al., Benchmark on Deterministic Transport Calculations without Homogenization, Nuclear energy agency organization for economic co-operation and development (NEA-OECD), 2003.
[28] B. Kong, K. Zhu, et al., Convergence study of DGFEM SN based 2D/1D coupling method for solving neutron transport k-eigenvalue problems with Fourier analysis, Ann. Nucl. Energy 177 (2022), 109327.
[29] Hyun Chul Lee, et al., Fourier convergence analysis of two-dimensional/one-dimensional coupling methods for the three-dimensional neutron diffusion eigenvalue problems, Nucl. Sci. Eng.J. Am. Nucl. Soc. 156 (1) (2014) 74–85.